

Theoretical modeling of Comptonized X-ray spectra of super-Eddington accretion flow: origin of hard excess in Ultraluminous X-Ray Sources

Takaaki KITAKI,^{1,*} Shin MINESHIGE,¹ Ken OHSUGA,² and Tomohisa KAWASHIMA²

¹Department of Astronomy, Graduate School of Science, Kyoto University,
Kitashirakawa-Oiwake-cho, Sakyo-ku, Kyoto 606-8502, Japan

²National Astronomical Observatory of Japan, 2-21-1 Osawa, Mitaka-shi, Tokyo 181-8588,
Japan

*E-mail: kitaki@kusasro.kyoto-u.ac.jp

Received (2017/May/31); Accepted (2017/Aug/27)

Abstract

X-ray continuum spectra of super-Eddington accretion flow are studied by means of Monte Carlo radiative transfer simulations based on the radiation hydrodynamic simulation data, in which both of thermal and bulk Compton scatterings are taken into account. We compare the calculated spectra of accretion flow around black holes with masses of $M_{\text{BH}} = 10, 10^2, 10^3$, and $10^4 M_{\odot}$ for a fixed mass injection rate (from the computational boundary at $10^3 r_s$) of $10^3 L_{\text{Edd}}/c^2$ (with r_s , L_{Edd} , and c being the Schwarzschild radius, the Eddington luminosity, and the speed of light, respectively). The soft X-ray spectra exhibit mass dependence in accordance with the standard-disk relation; the maximum surface temperature is scaled as $T \propto M_{\text{BH}}^{-1/4}$. The spectra in the hard X-ray bands, by contrast, look quite similar among different models, if we normalize the radiation luminosity by M_{BH} . This reflects that the hard component is created by thermal and bulk Compton scattering of soft photons originating from an accretion flow in the over-heated and/or funnel regions, the temperatures of which have no mass dependence. The hard X-ray spectra can be reproduced by a Wien spectrum with temperature of $T \sim 3$ keV accompanied by a hard excess at photon energy above several keV. The excess spectrum can be well fitted with a power law with a photon index of $\Gamma \sim 3$. This feature is in good agreement with that of the recent NuSTAR observations of ULX (Ultra-Luminous X-ray sources).

Key words: accretion, accretion disks — radiation: dynamics — stars: black holes

1 Introduction

It had been long believed that the classical Eddington limit can never be exceeded, as long as objects steadily shine by accreting environmental gas. Recently, however, there are growing evidences, which point the existence of astronomical objects shining at super-Eddington luminosities. Super-Eddington accretion flow is the flow, in which the accretion rate onto a cen-

tral object exceeds the classical limit which gives rise to super-Eddington luminosities; that is,

$$\dot{M} > \dot{M}_{\text{Edd}}/\eta \equiv L_{\text{Edd}}/(\eta c^2) \simeq 10^{19} (\text{g s}^{-1}) (\eta/0.1)^{-1} (M_{\text{BH}}/10 M_{\odot}), \quad (1)$$

where L_{Edd} is the Eddington luminosity, η (~ 0.1) is the energy conversion efficiency, M_{BH} is the black hole mass, and c is the

speed of light.

One of the best candidates of the super-Eddington accretors is Ultra-Luminous X-ray sources (ULXs), bright off-nuclear compact X-ray sources with luminosities of 10^{39} – 10^{41} erg s $^{-1}$, found in nearby galaxies. There are two major scenarios explaining the high luminosities of ULXs: sub-Eddington accretion to intermediate-mass black holes (e.g., Makishima et al. 2000; Miller et al. 2004), and super-Eddington accretion to stellar mass black holes (e.g., Watarai et al. 2001; King et al. 2001).

The discovery of X-ray pulses in M82 X-2 by Bachetti et al. (2014) was striking in this respect, since it demonstrates that the central star in M82 X-2 should be a neutron star and is thus less massive than $3M_{\odot}$. Super-Eddington accretion should, hence, be required to explain its high luminosity over 10^{40} erg s $^{-1}$. The discovery such an object called a ULX pulsar provides a good support for the existence of super-Eddington accretion in the universe. Two other ULX pulsars were discovered afterward (NGC7793 P13, Fürst et al. 2016; NGC5907 ULX, Israel et al. 2017).

We should note that ULXs are not the only super-Eddington accretors but there exist other sites, where super-Eddington accretion is going on. Some of microquasars are suspected to have super-Eddington accretion flow (see, e.g., Done, Gierlinski, & Kubota 2007) and some quasars at high (cosmological) redshifts are another example. Mortlock et al. (2011) discovered the quasars at the redshift, $z = 7.085$. Its black hole mass is estimated to exceed $10^9 M_{\odot}$. If this supermassive black hole had grown up from a population III remnant (a black hole with $M_{\text{BH}} \sim 10$ – $10^3 M_{\odot}$), super-Eddington accretion flows is inevitable, since otherwise the growth time to produce the observed supermassive black hole exceeds the age of the universe.

The inflow/outflow gas dynamics and emission properties of super-Eddington accretion have been extensively studied in this decade by means of multi-dimensional radiation hydrodynamic (RHD) simulations, being pioneered by Ohsuga et al. (2005) (see also Ohsuga et al. 2009, Ohsuga & Mineshige. 2011 for radiation-MHD simulations). More recently, general relativistic (GR) RHD simulations have been performed (Sądowski et al. 2014, 2015b; McKinney et al. 2014; Takahashi et al. 2016). They all demonstrated that significant fraction of inflow material is blown away by strong radiation-pressure force in forms of optically Thomson-thick, moderately high-temperature (\sim several keV) disk wind. Jiang, Stone & Davis (2014) have re-confirmed such a structure by modified RHD simulations. The emergent spectra should thus suffer Comptonization effects by the wind. Kawashima et al. (2012) were the first to calculate such Comptonized spectra of super-Eddington accretion flows and have shown that the theoretical spectra can well fit the typical ULX spectra in the X-ray band (Kawashima et al. 2009, 2012). They also notice that not only thermal Comptonization but also bulk Comptonization by wind motion plays a crucial

role in spectral formation. Quite recently Narayan et al. (2017) solved the GR radiative transfer problem by post-processing GR radiation magnetohydrodynamic (RMHD) simulations and obtained similar results. The presence of massive outflow was also pointed out from the observational points of view by Gladstone, Roberts, & Done (2009) and Middleton et al. (2015b).

We here make more extensive study of Comptonized spectra expected from super-Eddington accretion flow for a variety of black hole masses and see how the spectra depend on the black hole mass and the viewing angle. So far the theoretical efforts have been focused on clarifying how the spectra depend on mass accretion rate, while the black hole mass dependence of that flows has been poorly investigated. In addition, we pay particular attention to the detailed spectral shape in the hard X-ray ranges. Now is a good time to perform such study, since thanks to NuSTAR we now have rich data of hard X-ray emission spectra of ULXs with good resolution. The organization of the paper is as follows: we first explain our model and methods of calculations in section 2 and then show our results in section 3. The final section is devoted to discussion and conclusions.

2 Numerical Method

2.1 Radiation Hydrodynamic Simulations of Supercritical Accretion Flows

In the present study, we perform spectral calculations based on the two-dimensional (2D) radiation hydrodynamic (RHD) simulation data, in which both of bulk and thermal Comptonization are taken into account (Pozdnyakov et al. 1983). This 2D RHD code solves the axisymmetric two-dimensional radiation hydrodynamic equations in the spherical coordinates. The flux-limited diffusion approximation is adopted (Levermore & Pomraning 1981; Turner & Stone 2001), and general relativistic effects are incorporated by adopting the pseudo-Newtonian potential (Paczynski & Wiita 1980). We also adopt the α viscosity prescription (Shakura & Sunyaev 1973) and we set $\alpha = 0.1$.

Basic equations and numerical methods are the same as those in Kawashima et al. (2009, 2012). Simulation settings are roughly the same as those in Kawashima et al. (2012). The computational domain of the radiation hydrodynamic simulations is described by $r_{\text{in}} = 2r_s \leq r \leq r_{\text{out}} = 1000r_s$, and $0 \leq \theta \leq \pi/2$. Here $r_s = 2GM_{\text{BH}}/c^2$ is the Schwarzschild radius with G being the gravitational constant. Grid points are distributed according to the radial and azimuthal coordinates and each grid spacing is $\Delta \log_{10} r = (\log_{10} r_{\text{out}} - \log_{10} r_{\text{in}})/N_r$ and $\Delta \cos \theta = 1/N_{\theta}$, respectively, where the numbers of grid points are taken to be $(N_r, N_{\theta}) = (192, 192)$ throughout the present study.

We start calculations with an empty space but for numerical reasons we initially put hot, rarefied, and an optically thin atmosphere. Mass is injected continuously with a constant rate of

$\dot{M}_{\text{input}} = 10^3 L_{\text{Edd}}/c^2$ through the outer boundary at $r = r_{\text{out}}$ and $0.45\pi \leq \theta \leq 0.5\pi$. We set that the injected matter has an angular momentum corresponding to the Keplerian angular momentum at $r = 300r_s$. The matter can go out freely through the boundary $r = r_{\text{out}}, 0 \leq \theta \leq 0.45\pi$, and the absorbing boundary condition is adopted at $r = r_{\text{in}}$.

The black hole mass is a free parameter and is set to be $M_{\text{BH}} = 10^1 M_{\odot}, 10^2 M_{\odot}, 10^3 M_{\odot}$, and $10^4 M_{\odot}$. (The previous study by Kawashima et al. 2012 solved only the case with $M_{\text{BH}} = 10 M_{\odot}$.)

2.2 Monte Carlo Calculations of Radiative Transfer

The code which we use for the spectral calculation is that developed by Kawashima et al. (2012). This three dimensional Monte Carlo simulation code (hereafter 3D MC code) solves the three-dimensional radiative transfer by means of the Monte Carlo method by post-processing the simulation data produced by the 2D RHD code described above. Before spectral calculations we time average gas mass density, temperature, and velocity at each grid point for every $0.25 M_{\text{BH}}/M_{\odot}$ sec. We only use the data after accretion flows become quasi-steady.

The 2D RHD simulations data given in terms of the spherical coordinates are converted to the data in the Cartesian coordinates by interpolation. The computational domain of the radiative transfer calculations is set by $-300r_s \leq x, y, z \leq 300r_s$ and the numbers of the grid points are $(N_x, N_y, N_z) = (160, 160, 160)$. In the quasi-steady accretion regime, the accretion rate onto the central black hole, which we calculate by summing up mass passing through the inner boundary at $r = r_{\text{in}}$, is approximately $\dot{M} \sim 200 L_{\text{Edd}}/c^2$. Since the mass input rate through the outer boundary is $10^3 L_{\text{Edd}}/c^2$, about 80% of input material is wandering or being drawn away out of the computational domain.

The photosphere is set up $\tau_{\text{eff}}(\nu) = \sqrt{3\tau_a(\nu)(\tau_a(\nu) + \tau_e)} = 10$ calculated along z -axis direction from $z_{\text{max}} = 300r_s$ to $-z_{\text{max}}$ (with τ_a and τ_e being the absorption optical depth and the electron scattering optical depth, respectively). Here, we only consider bremsstrahlung absorption for evaluating τ_a .

At each frequency bin the seed photons, of which the number is 6×10^5 , are generated within a $\tau_{\text{eff}}(\nu) < 10$ region. In this region the generation point of each photon is selected such that the generated photon number per unit volume is proportional to the local bremsstrahlung emissivity. We consider free-free absorption and bulk & thermal Comptonization effects to describe the interaction between photons and matter. The black hole swallows photons which go through $r < 2r_s$. The spectrum frequency setting is $\nu_{\text{min}} = 10^{14} \text{ Hz} < \nu < \nu_{\text{max}} = 10^{21} \text{ Hz}$ with $\Delta \log_{10} \nu = (\log_{10} \nu_{\text{max}} - \log_{10} \nu_{\text{min}})/100$.

3 Results

3.1 Overall flow structure

We first overview the flow structure by inspecting the 2D density and temperature distributions of each model. The top four panels in Figure 1 show the time-averaged density contours for the black hole mass of $M_{\text{BH}} = 10^1, 10^2, 10^3$, and $10^4 M_{\odot}$ from the left to the right, respectively.

We find a quite similar color contour pattern in every top panel, as long as the length scale and the density are normalized by $r_s (\propto M_{\text{BH}})$ and by $\rho (\propto M_{\text{BH}}^{-1})$, respectively. Common features to all the top panels are that the flow consists of a high-density inflow part (or a disk) around the equatorial plane (indicated by the red-to-yellow color) and a low-density outflow part (or a funnel region) around the rotational axis (indicated by the blue color). Note that the former disk part can be well modeled by a geometrically thick accretion disk.

The density dependence on M_{BH} can be understood in the following way: Let us scale other relevant quantities in terms of the black hole mass; e.g., velocity by free-fall velocity, $v_{\text{ff}} = c(r/r_s)^{-1} \propto M_{\text{BH}}^0$, luminosity by $L_{\text{Edd}} \propto M_{\text{BH}}$, and mass accretion rate by $\dot{M}_{\text{Edd}} = L_{\text{Edd}}/c^2 \propto M_{\text{BH}}$. From the continuity equation, we have $r^2 \rho v_r \propto \dot{M} (\propto M_{\text{BH}})$. We finally obtain $\rho \propto M_{\text{BH}}^{-1}$.

The bottom four panels in Figure 1 show time-averaged gas temperature distribution. Again, all the four panels look similar except in the inflow region around the equatorial plane, where we find higher temperatures in the left panels than in the right panels. This difference can be easily understood, since the temperature of accretion disk is proportional to $M_{\text{BH}}^{-1/4}$ (detailed explanation will be provided later). While the temperature in other regions, especially in the funnel region, is insensitive to the black hole mass.

For readers' convenience we specify in figure 2 the precise locations of the three key regions: disk, funnel, and over-heated region. This figure is an enlarged snapshot of the temperature contours and corresponds to the bottom left panel of figure 1, although the panels in figure 1 are not snapshots but time-averaged pictures. It is important to note that an abrupt heating occurs where the inflow material collides with the funnel wall. The highest temperature part (with $T \sim 10^8 \text{ K}$) is produced near the black hole because of abrupt heating and it is this region plays an essential role in hard photon production (Kawashima et al. 2012).

The disk and funnel regions are distinguished in terms of the directions of the gas motion, temperature, and the density (or optical depth). Thomson optical depth of the funnel region is:

$$\tau_e = \int_{z_{\text{wall}}}^{z_{\text{max}}} \sigma_T \rho dz \sim 1. \quad (2)$$

Here, σ_T is Thomson cross section, z_{max} is the boundary of computational box, and z_{wall} is the z -position of funnel wall.

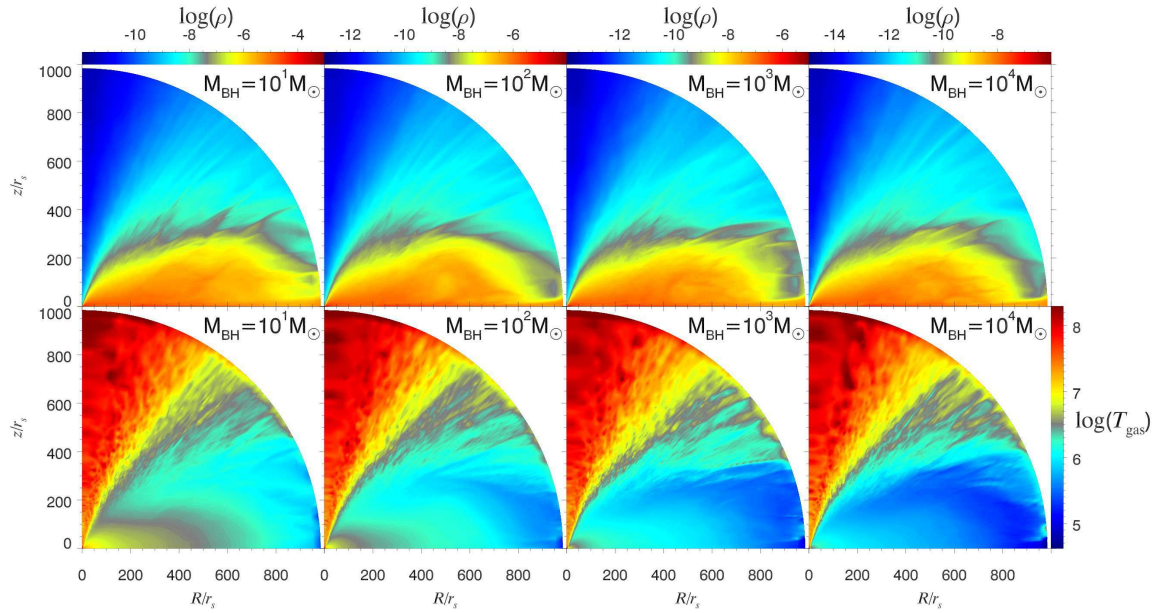


Fig. 1. [Top panels] Time-averaged density contours of super-Eddington accretion flow onto black holes with masses of $M_{\text{BH}} = 10^1, 10^2, 10^3$, and $10^4 M_{\odot}$ from the left to the right, respectively. All the panels look similar, if we change the color scale according to the density normalization, $\rho \propto M_{\text{BH}}^{-1}$. [Bottom panels] The same as those in the upper panels but for the time-averaged gas temperature distributions. The color scales are the same in all the panels.

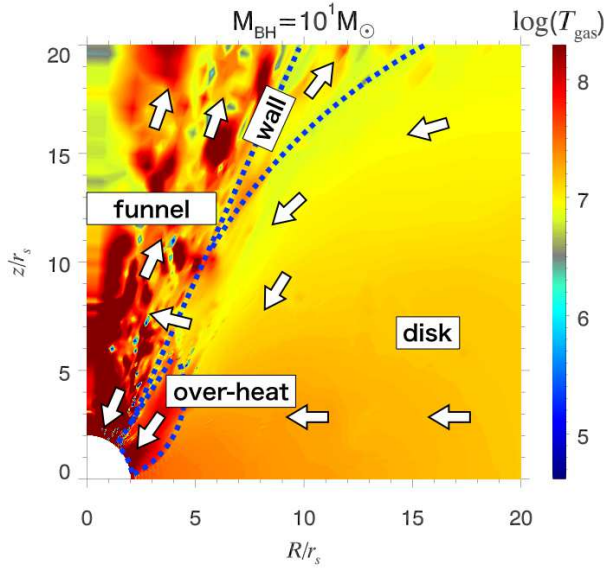


Fig. 2. Enlarged snapshot of gas temperature contours close to the black hole at $t = 6.04\text{s}$ for model with $M_{\text{BH}} = 10 M_{\odot}$. Overlaid are arrows which represent the direction of gas motion. (Note that the lengths of the arrows are not in scale.) The three key regions are separated by the blue dash lines: accretion flow around the equatorial plane (indicated by 'disk'), funnel region near the polar axis (indicated by 'funnel'), and the over-heated region (indicated by 'over-heat'). The location of the funnel wall is also indicated in this figure (by 'wall').

The opening angle of funnel is roughly $\theta_{\text{open}} \sim 20^\circ - 25^\circ$.

Different mass dependences of the two regions can be understood as follows: To demonstrate that the disk temperature at a

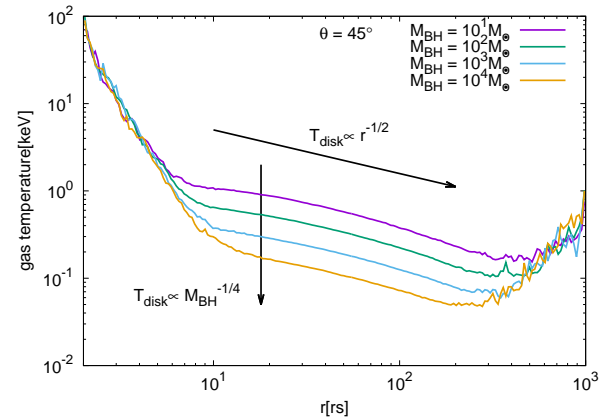


Fig. 3. The gas temperature depending on radius ($\theta = 45^\circ$ from z -axis) for models with $M_{\text{BH}} = 10^1, 10^2, 10^3, 10^4 M_{\odot}$.

fixed radius does have a mass dependence of $T_{\text{disk}} \propto M_{\text{BH}}^{-1/4}$, we have checked the radial profiles of the disk temperature by using the simulation data (e.g. figure 3), confirming the relationship of $T_{\text{disk}} \propto M_{\text{BH}}^{-1/4} \times (r/r_s)^{-1/2}$. This mass dependence is the same as that of the standard disk, while the radial dependence is not. We can simply understand this results in the following way (Kato et al. 2008, equation 10.22): The surface temperature of a standard-type disk at a fixed r/r_s obeys

$$\sigma T_{\text{disk}}^4 \sim \frac{3}{8\pi} \frac{GM\dot{M}}{r^3} \propto M_{\text{BH}}^{-1} \left(\frac{r}{r_s}\right)^{-3}, \quad (3)$$

leading to $T_{\text{disk}} \propto M_{\text{BH}}^{-1/4} (r/r_s)^{-3/4}$, as long as we assume $\dot{M} \propto M_{\text{BH}}$. In the supercritical flow, by contrast, the temperature profile of the disk no longer depends on the mass accretion

rate. Then, the disk temperature at a fixed r/r_s obeys

$$\sigma T_{\text{disk}}^4 \sim \frac{L_{\text{Edd}}}{2\pi r^2} \propto M_{\text{BH}}^{-1} \left(\frac{r}{r_s}\right)^{-2}, \quad (4)$$

leading to $T_{\text{disk}} \propto M_{\text{BH}}^{-1/4} (r/r_s)^{-1/2}$. Therefore, the supercritical disk has the same mass dependence as that of the standard disk [Eq. (3)].

In the high-temperature funnel region ($5r_s \lesssim r \lesssim 100r_s$ and $0^\circ \leq \theta \lesssim 20^\circ$), on the other hand, radiative viscous heating balances with Compton cooling. That is, by equating

$$\Phi_{\text{vis}} = \eta \left(r \frac{\partial \Omega}{\partial r} \right)^2 \sim \alpha E_0 \Omega_K \left(\frac{\Omega}{\Omega_K} \right)^2 \left(\frac{\partial \ln \Omega}{\partial \ln r} \right)^2, \quad (5)$$

and

$$\Gamma_{\text{comp}} \sim 4\sigma_T c \frac{k_B T_{\text{funnel}}}{m_e c^2} \left(\frac{\rho}{m_p} \right) E_0, \quad (6)$$

we have

$$k_B T_{\text{funnel}} \sim \frac{\alpha}{2} m_e c^2 \frac{m_p}{\rho \sigma_T r_s} \left(\frac{v_\phi}{c} \right)^2 \left(\frac{r}{r_s} \right)^{-\frac{1}{2}} \left(\frac{\partial \ln \Omega}{\partial \ln r} \right)^2. \quad (7)$$

We hence see that the right-hand side has no mass dependence, so does the funnel temperature.

Numerically, we find $\sim 10^7$ K from equation (7) and this temperature is in good agreement with that of the funnel wall located along the line of $\sim 20^\circ$ from the rotation axis (see figure 2). The gas temperature within the funnel is by a factor of several to ten times greater than the above estimation. This is probably because the gas within the funnel had been heated when passing through the over-heated region. We should also point out that the heating process within the funnel may not be so accurately described by the α viscosity prescription. This point will be improved by future MHD simulations.

The temperature in the over-heated region is about $T_{\text{heat}} \sim 10^8$ K regardless of the black hole mass (see figure 2 and also 1), as is expected from the relation that kinetic energy is converted to internal energy; that is, from

$$\frac{1}{2} \rho v^2 \propto (\gamma - 1) \frac{\rho k_B T_{\text{heat}}}{\mu m_p}, \quad (8)$$

we have

$$k_B T_{\text{heat}} \propto \frac{\mu m_p v^2}{2(\gamma - 1)} \propto M_{\text{BH}}^0, \quad (9)$$

Note that the inflow velocity v is independent black hole mass. In reality the temperature of the over-heated region is much lower than this simple estimation because of significant Compton cooling by soft photons emerging from the underlying accretion flow (with temperature of $T_{\text{disk}} \sim 10^7$ K for $M_{\text{BH}} = 10 M_\odot$).

3.2 Emergent radiation spectra

Figure 4 shows total spectra viewed by a distant face-on observer and its dependence on the black hole mass: $M_{\text{BH}} = 10^1, 10^2, 10^3$, and $10^4 M_\odot$. Here, by a face-observer we mean

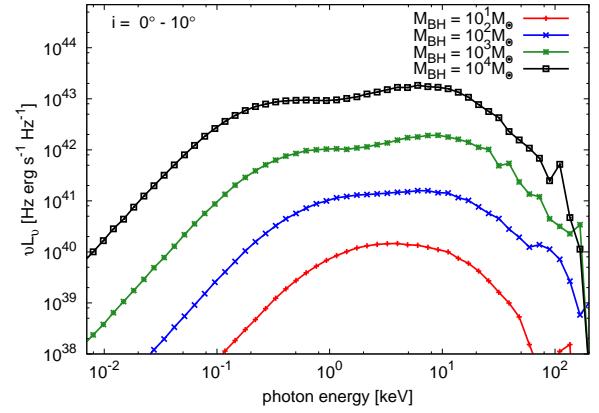


Fig. 4. Calculated spectra viewed from the angle of $i = 0^\circ - 10^\circ$ from the polar angle for the black hole masses of $M_{\text{BH}} = 10^1, 10^2, 10^3$, and $10^4 M_\odot$. The mass accretion rate is fixed to be $\dot{M} = 10^3 L_{\text{Edd}}/c^2$. The non-monotonic variations in the hard X-ray ($\gtrsim 10$ keV) are due to noise arising from insufficient number of photons used in the Monte Carlo methods.

an observer viewing from the angle between $i = 0^\circ - 10^\circ$ from the rotation axis.

There are some noteworthy features seen in figure 4. First, the larger black hole mass is, the brighter becomes the flow. This is because we fixed the mass accretion rate in terms of M_{BH} and, hence, the luminosity of super-Eddington accretion flows is roughly proportional to the Eddington luminosity, $\nu L_\nu \sim L_{\text{Edd}} \propto M_{\text{BH}}$.

Second, the overall spectral shape in the hard X-ray bands looks quite similar, if we normalize the radiation intensity by M_{BH} . In other words, the peak frequency of the hard component remains the same. This is a direct consequence that the temperature of the hard X-ray emitting regions is insensitive to the black hole mass; $T_{\text{funnel}} \propto M_{\text{BH}}^0$ (see the previous subsection). The spectral rollover at $h\nu_{\text{peak}} \sim 7$ keV can be understood, if the photons from the disk region is once over-heated and is then Compton cooled by the gas at the funnel wall (with $\sim 10^7$ K).

Finally, the soft X-ray spectra have a mass dependence. That is, the higher the black hole mass is, the higher becomes the soft X-ray luminosity, and the lower becomes the spectral break between the Rayleigh-Jeans part and the flat spectrum part ($h\nu_{\text{break}} \propto k_B T_{\text{disk}} \propto M_{\text{BH}}^{-1/4}$). The luminosity in the Rayleigh-Jeans range obeys $\nu L_\nu \propto M_{\text{BH}}^{7/4}$, since from

$$T(R) \equiv T_0 \left(\frac{R}{r_s} \right)^{-p} \quad \text{with } T_0 \propto M_{\text{BH}}^{-1/4}, \quad (10)$$

we find

$$F_\nu \propto \int_{R_{\text{in}}}^{R_{\text{out}}} 2\pi R B_\nu dR \quad (11)$$

$$= \frac{4\pi\nu^2 k_B T_0 r_s^2}{c^2} \int_{R_{\text{in}}/r_s}^{R_{\text{out}}/r_s} \left(\frac{R}{r_s} \right)^{1-p} d\left(\frac{R}{r_s} \right) \quad (12)$$

$$\propto T_0 r_s^2 \propto M_{\text{BH}}^{7/4} \quad (\text{for } h\nu \ll k_B T_0) \quad (13)$$

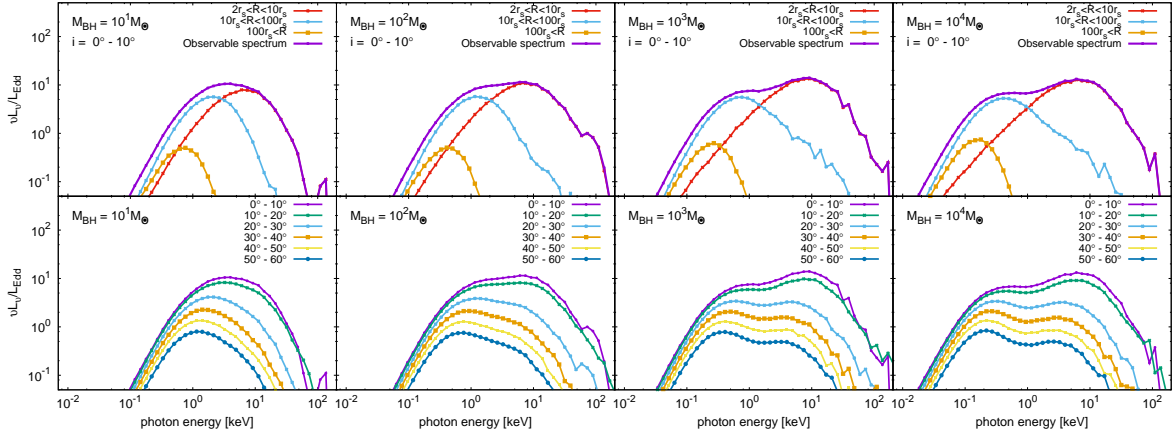


Fig. 5. [Top panels] Total emission spectra viewed from the angle of $i = 0^\circ - 10^\circ$ (the purple line) and the contributions to the total spectra by different zones: by the inner region between $2r_s < R < 10r_s$ (the red line), by the middle region between $10r_s < R < 100r_s$ (the blue line), and by the outer region between $R > 100r_s$ (the yellow line) for the black hole mass of $M_{\text{BH}} = 10^1, 10^2, 10^3$, and $10^4 M_\odot$, from the left to the right, respectively. [Bottom panels] The same as the top panels but show the viewing angle dependence of the spectra. The non-monotonic variations in the hard X-ray ($\gtrsim 10$ keV) are due to noise arising from insufficient number of photons used in the Monte Carlo methods.

(Here, R_{in} and R_{out} are the radii of the inner and outer edges of the accretion disk, respectively. and we assumed that both radii are scaled in terms of r_s .) This dependence is in good agreement with the simulation results shown in figure 4. For these reasons the spectrum is roughly the summation of the high- and low-temperature blackbody emissions.

Figure 5 displays decomposition of the total emission spectra according to the regions where photons are originally generated. Here we divide the total flow region into the three: the inner region ($2r_s < R < 10r_s$), the middle region ($10r_s < R < 100r_s$), and the outer region ($R > 100r_s$). Here, R is the radial coordinate in the cylindrical coordinates $R = \sqrt{x^2 + y^2}$.

From this figure we understand that the observable spectrum is mainly composed by direct soft photons from accretion disk and hard photons which are Compton up-scattered near the black hole. But we see a hard X-ray rollover at around 7 keV which arises due to the Compton down-scattering in low temperature outflow (Kawashima et al. 2012). This issue (regarding the origin of hard X-rays) will be discussed in more details in the next section.

The bottom four panels in Figure 5 show the viewing-angle dependence of the emergent spectra for each model. The larger the viewing angle is, the weaker the hard X-ray flux becomes. This is because an observer viewing from large angles is hard to see directly funnel near the black hole ($z \lesssim 30r_s$). We can thus explain the very soft X-ray spectra of ULSs (Ultra-Luminous Supersoft sources; see Gu et al. 2016, Ogawa et al. 2017).

4 Discussion

4.1 Brief summary

In the present study we elucidate the spectral properties of the super-Eddington accretion flow and outflow by means of the three dimensional Monte Carlo radiation transfer simulation based on the global 2D RHD simulation data. The purpose of the present study is two-fold: (1) to extend the study by Kawashima et al. (2012) for a variety of black hole masses, and (2) to calculate more accurate hard X-ray spectra. Regarding the first issue, we have seen remarkably similar flow structure and overall spectral properties, especially in the hard energy bands. The detailed inspection of the hard spectral component (the second issue) is made possible by increasing photons used in the Monte Carlo simulations. We find a significant excess over the exponential rollover above several keV. This should be a result of complex, multiple Compton scattering of photons within the over-heated region, as well as in the funnel region. We admit the limitations of the present RHD simulations, since MHD processes are not properly solved there. Definitely, we need radiation-MHD simulation in future work to calculate more precisely flow temperature and radiation spectra.

In the following subsections we make more detailed study how photons finally acquire high energy by multiple Compton scatterings, interacting with high-temperature or high-velocity plasmas.

4.2 How is the power-law component constructed?

In figure 4 we have already seen the excess component in the hard X-ray energy range (above several keV). One possible origin for creating power-law photons is unsaturated

Table 1.

place	quantities (unit)	numerical values
photon generation	photon energy (keV)	$1.0(+1.2/-1.0)$
	R -coordinate (r_s)	4.6 ± 2.6
	z -coordinate (r_s)	2.0 ± 1.4
maximum energy	photon energy (keV)	100 ± 85
	gas temperature (keV)	13 ± 9.2
	gas velocity (c)	0.28 ± 0.07
	R -coordinate (r_s)	2.2 ± 2.2
	z -coordinate (r_s)	$3.4(+5.8/-3.4)$
last scattering	energy amplification* ¹	1.1 ± 0.34
	gas temperature (keV)	1.7 ± 0.65
	gas velocity (c)	0.19 ± 0.11
	R -coordinate (r_s)	$11(+16/-11)$
	z -coordinate (r_s)	$32(+41/-32)$

Statistical properties of hard photons (with final energy above 10 keV) which reach an observer viewing from the angles between $i = 0^\circ - 10^\circ$ for the case with $M_{\text{BH}} = 10M_\odot$. Generated soft photons are once heated up to several tens of keV at maximum near the black hole and are then Compton cooled down to be observed. *¹ Ratio of the photon energy before to that after the last scattering.

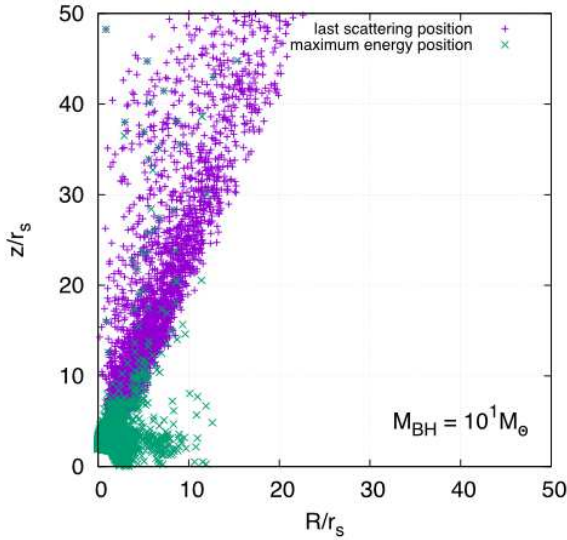


Fig. 6. The positions where each hard photon (with final energy above 10 keV) suffers a last scattering before reaching a distant face-on observer (by the purple pluses +) and those where the same photons reach their maximum energy before the last scattering (by the green crosses x). Here, we consider the case with the black hole mass of $M_{\text{BH}} = 10M_\odot$.

Comptonization (e.g. Rybicki & Lightman 1979), since we estimate the electron scattering optical depth to be $\tau_{\text{es}} \gg 1$ because of very high density, whereas the Compton y -parameter [$y \equiv (4k_B T/m_e c^2) \max(\tau_{\text{es}}, \tau_{\text{es}}^2)$] moderately exceeds unity (around several to 10).

In order to understand the origin of hard photons we check the trajectories and energy variation histories of the hard photons. We set two conditions to select hard photons; (1) their final energy should exceed 10 keV and (2) they should eventually be observed by a distant face-on observer.

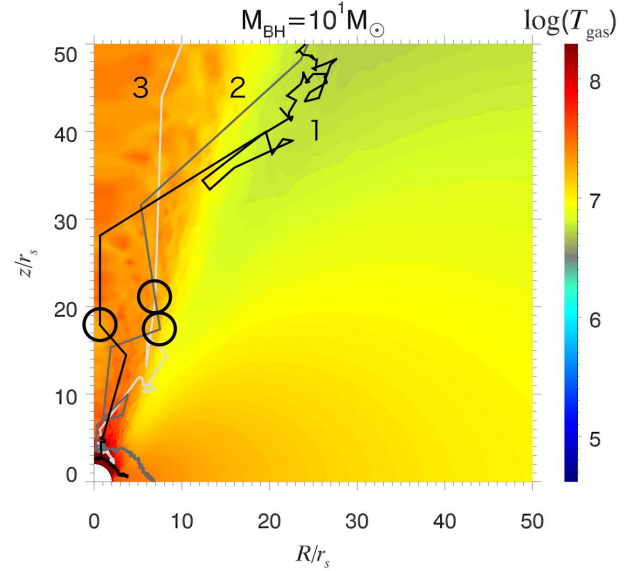


Fig. 7. Trajectories of the three representative photons on the (R, z) plane overlaid with gas temperature contours. The indices 1, 2, and 3 correspond to those in Figure 8. Photons escape to observer on the viewing angle $i = 0^\circ - 10^\circ$ at black circle.

The results are summarized in Figures 6 – 8 for the case with $M_{\text{BH}} = 10M_\odot$ (see also Table 1). From these we confirm the following facts:

1. These hard photons were generated as soft photons with ~ 1 keV within the inflow region around the equatorial plane; $R \lesssim 10r_s$ and $z \lesssim 5r_s$.
2. After the generation these photons travel around the black hole for a while, being scattered many, many times.
3. The photons then go into the over-heated region (see figure 2 in section 3). In this region, optical depth and electron temperature are $\tau_e \approx 10$ and $k_B T_e \approx 8.6$ keV, respectively, while the Compton y parameter is very large; $y \approx 7$. The photons are thus Compton up-scattering many times within the over-heated region so that they can acquire large energy to become hard photons.
4. These hard photons then eventually reach the foot-point of the funnel and enter the funnel region, where gas is accelerated upward by radiation-pressure force and thus has a large radial velocity, up to $\beta = v/c \sim 0.2$, near the funnel wall.
5. Within the funnel the hard photons experience Compton up- and down-scatterings. After passing through the funnel wall, some photons escape to directly reach the observer, while some others are reflected by the wall, return to the funnel region and are Compton down-scattered there again, and finally goes out of the funnel region to reach the observer as soft photons.

To summarize, the hard photon production processes are too complex to simply describe. The observed hard power-law

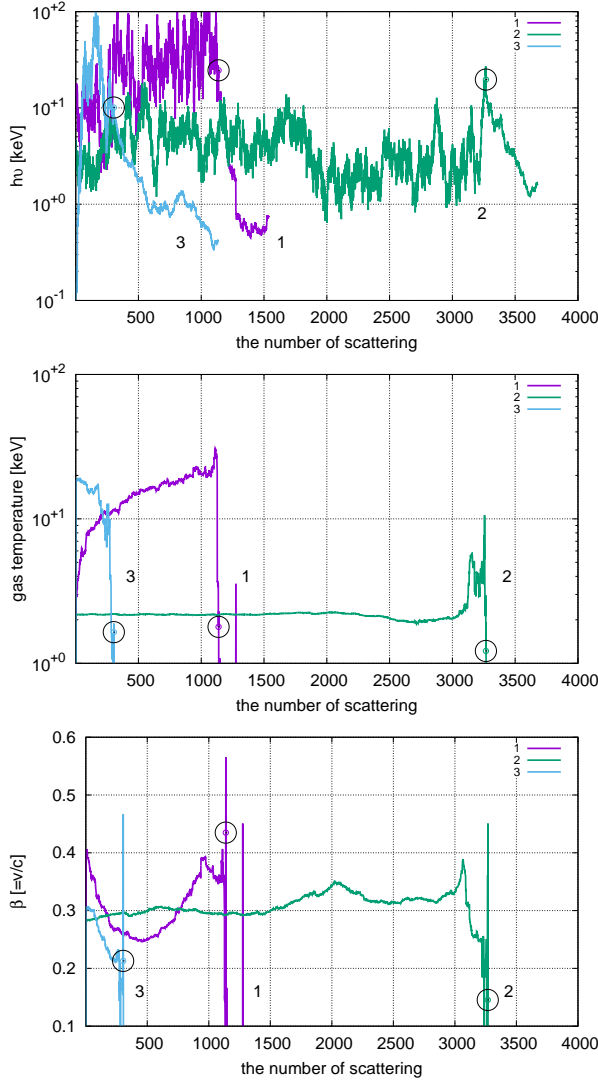


Fig. 8. Photon energy, gas temperature, and gas velocity variations which the three photons displayed in figure 7 experience as functions of the number of scattering. Note that the indices, 1, 2, and 3 correspond to those in Figure 7. Photons escape to observer on the viewing angle $i = 0^\circ - 10^\circ$ at black circle.

spectra are formed as a consequence of such complex matter-photon interactions.

As Kawashima et al. (2012) claimed, not only the thermal Comptonization but also the bulk Comptonization play important roles in the formation of hard X-ray spectra (see their fig. 5). The speed of the outflow that photons encounter is around $\beta \equiv v/c \sim 0.2$ (see table 1). Since the photon energy amplification factor is from Pozdnyakov et al. (1983)

$$\frac{\Delta(h\nu)}{h\nu} = \frac{\frac{4}{3}\beta^2\gamma^2 m_e c^2 - h\nu}{m_e c^2}. \quad (14)$$

we estimate that the photon energy can acquire energy at most around $h\nu \sim \frac{4}{3}\beta^2\gamma^2 m_e c^2 \sim 30(\beta/0.2)^2$ keV. For $\beta = 0.1 - 0.3$ we find $h\nu \simeq 8 - 70$ keV.

4.3 The effects of iterated temperature, magnetic field, and general relativity.

We do not recompute the temperature in their simulations using the Monte Carlo code, although this is sometimes implemented by others using similar methods (e.g. Narayan et al. 2017). Here, we calculate what the “correct” temperature would be, if we would use the calculated radiation spectra as a source of Compton cooling. For this purpose, we check the temperature of the photosphere at around $(R, z) = (11r_s, 32r_s)$, from which hard X-ray (> 10 keV) photons mainly come from, finding that the mean photon energy is $\langle h\nu \rangle \sim 14.9$ keV. This energy corresponds to the radiation temperature of $k_B T_{\text{rad}}^1 = \langle h\nu \rangle / 4 \sim 3.7$ keV. On the other hand, the gas temperature found in the original RHD simulation is $k_B T_{\text{gas}}^0 \sim 1.2$ keV. Therefore, we have $T_{\text{gas}}^0 < T_{\text{rad}}^1$, meaning that gas should be Compton heated by radiation. However, we should point that bulk Compton is dominant over the thermal Compton even for this recalculated temperature; i.e., $v_{\text{thermal}}/c \sim \sqrt{3k_B T_{\text{gas}}^1/m_e c^2} \sim 0.147$ (assuming $k_B T_{\text{gas}}^1 \sim k_B T_{\text{rad}}^1$), while the bulk velocity is $v_{\text{bulk}}/c \sim 0.2$. We can thus safely conclude that the iterated temperature can hardly affect the hard X-ray emission properties discussed in the present paper.

We consider why recomputation of the temperature is not so critical in our simulations unlike the simulations by Narayan et al. (2017). Narayan et al. (2017) mentioned that the gas temperature (before the recomputation) is very high around the rotation axis since the Compton-cooling is less effective. The cause of that is the deficit of the radiation induced by the M1-closure method. The M1 method tends to suppress the radiation energy density around the axis via the artificial centrifugal shocks (Sądowski et al. 2013; 2015a). Thus, after recomputation, the high gas temperature ($\sim 10^9$ K) is significantly reduced to about 10^8 K by the effective Compton cooling. In contrast, artificial reduction of the radiation energy density around the axis does not occur in the FLD approximation method that is employed in the present work. Hence, the gas temperature near the polar axis may be already low, about 10^8 K. In addition, the relatively low gas temperature in the region far from the polar axis is nearly the same as those reported by Narayan et al. (2017). In this region, the gas temperature does not change so much by the recomputation. For these reason, our spectra look quite similar to those in Narayan et al. (2017).

The differences in methods (MHD versus non-MHD, general relativity versus no general relativity) are surprisingly small. To check if this is true, we first estimate the effects of the gravitational redshift. The spectrum is reproduced by multiplying the redshift to the photon energy at only last scattering position. The redshift is very important near the black hole, but in that place, photons are many Compton scattered. Then it seems to be sufficient to consider the redshift at the last scattering position. There is no significant difference between spectrum, e.g.

sed(no redshift)/sed(redshift) $\sim 0.98 - 1.2$ each photon energy. This is because the location of the last scattering surface of the hard X-ray is quite far from the black hole. For this reason, we conclude that our spectrum (non-GR) is almost same as Narayan et al. 2017 (GR).

We next check how important magnetic effects are. It is important in this context to point out the inequality of radiative-pressure $>$ gas-pressure $>$ magnetic-pressure in the funnel region, which was first pointed out by radiation-MHD simulations by Ohsuga & Mineshige. (2011). The effects of the magnetic field seem to be weak and spectrum is almost same between MHD and non-MHD. However, magnetic dissipation could be more enhanced above or near the photosphere, rather than in the equatorial region. It is thus necessary to check if this is the case in future radiation-MHD simulations.

We further estimate the effects of cyclotron emission and absorption as follows: There are two regions in which magnetic field is relatively strong: the funnel region and the region very close to the black hole. In the funnel region, first of all, the magnetic field strength is $B \sim 10^5$ G (Ohsuga & Mineshige. 2011). The gas velocity is up to $v < 0.5c$, and the Lorentz factor is $\gamma \sim 1$. The typical frequency of cyclotron is $\nu_g = eB/(2\pi m_e c) \sim 3 \times 10^{11}$ Hz, $\nu_{\text{crit}} = 3\gamma^2 \nu_g \sin \alpha/2 \sim \nu_g \sin \alpha < \nu_g$. In this frequency ν_{crit} , the cyclotron process does not emit and absorb X-ray.

In the region near the black hole ($R < 10r_s, z < 5r_s$), secondly, the magnetic field is $B \sim 10^8$ G (Ohsuga & Mineshige. 2011). In the same way, frequency is $\nu_g \sim 3 \times 10^{14}$ Hz, and so the cyclotron process does not absorb X-ray, and emit radio (or far-infrared) wave. The seed photon generated near the black hole in the disk are observed as hard X-ray through the Compton effect. But cyclotron radio emission does not become this seed photon because there are a lot of the seed photons by free-free emission (~ 1 keV) from the disk. For these reasons, our spectrum (non-MHD) looks like that by Narayan et al. 2017 (MHD).

It is, of course, possible that the flow structure might be somewhat altered, if we would incorporate the MHD and GR effects. Especially, the effects of MHD and GR would be important in magnetically arrested disks (MADs), and MADs around highly spinning BH, respectively. (We note that we have studied non-MADs around non-rotating BHs in this paper). For example, McKinney et al. (2017) carried out 3D GR-RMHD simulations of super-critically accreting MADs and found that the cyclo-synchrotron cooling is dominant in the jet and corona region. Narayan et al. (2017) found that the SEDs of MADs around a highly spinning BH differ from those of non-MADs or MADs around a non-spinning BH, because the speed of jets in MADs with highly spinning BH is higher than the others and that results in the decrease of the optical depth in the jet and leads high frequency photons emitted from the plasma near the

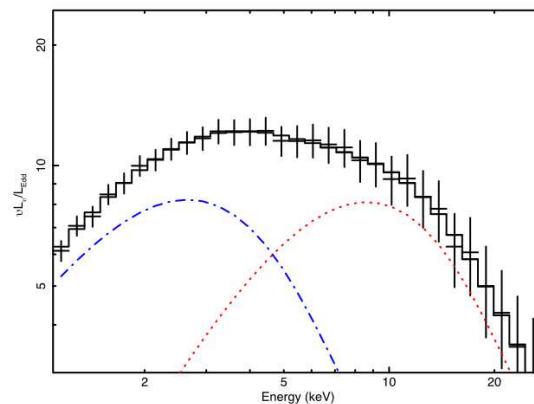


Fig. 9. Result of fitting to the theoretical spectrum displayed in figure 4 for the case with $M_{\text{BH}} = 10M_{\odot}$. The fitting function is the summation of two blackbody spectra associated with a power-law component (SIMPL * (DISKBB + DISKPBB)) in Xspec, same as that adopted in Walton et al. 2015 excluding the interstellar absorption (TBABS). The red dotted and blue dash-dotted curves, respectively, represent the best-fit high-temperature and low-temperature blackbody components. [More precisely, the former component is the p -free disk blackbody spectra, in which the disk surface temperature is scaled as $T_{\text{surface}} \propto r^{-p}$ with p being the fitting parameter; see Mineshige et al. 1994.]

Table 2.

Model	Parameter (unit)	numerical values
DISKBB	T_{in} (keV)	$1.0(\pm 0.49)$
DISKPBB	T_{in} (keV)	$3.1(+1.6/-1.1)$
	p	$0.87(+0.13/-0.27)$
SIMPL	Γ	$2.8(+2.2/-2.8)$

The fitting parameters obtained by Xspec for the case with $M_{\text{BH}} = 10M_{\odot}$ (see, Figure 9).

BH to be observable. It is our future work to calculate radiation spectra based on the GR-RMHD simulations.

4.4 Application to the ULXs

In figure 4 we show the observable photon energy spectrum which is to be observed by a face-on observer for the case with $M = 10M_{\odot}$. We find a significant excess over an exponential rollover in the hard X-ray range. This is quite reminiscent of the recent NuSTAR observations of ULXs. For example, Walton et al. (2015) reported a hard X-ray excess in the NuSTAR spectrum of Holmberg II X-1, one of the most extensively studied ULXs. They performed spectral fitting, finding that this excess component can be best-fit by a power-law component with the photon index of $\Gamma = 3.1^{+0.3}_{-1.2}$. They discuss that likely origin of this power-law tail is Comptonization of soft photons by a hot (or even non-thermal) coronal plasma.

To check to what extent our theoretical spectra can reproduce the observed ones, we perform similar spectral fittings to the theoretical one by using the same spectral models excluding TBABS (i.e., the model which X-ray is absorbed by interstel-

lar medium) as those used by Walton et al. (2015). The results are illustrated in figure 9. It clearly shows that the theoretical spectrum can nicely be represented by two blackbody-like components with a power-law tail (see also table 2 for the best-fit parameters). The most remarkable is the power-law photon index, $\Gamma \sim 3$, which is in good agreement with the NuSTAR observation of Ho II X-1 [$\Gamma = 3.1 (+0.3/-1.2)$]. The temperature of the higher temperature blackbody is ~ 3 keV, somewhat higher than the observed one [$1.8 (+0.7/-0.3)$ keV].

The temperature of the lower temperature one (~ 1.0 keV) is, on the other hand, significantly higher than the observed one [$0.20 (+0.03/-0.04)$ keV]. But this disagreement should not be taken seriously, since our computational box is not large enough to resolve the accretion flow structure at large radii, from where soft X-ray emission originates. We thus focus out discussion to the hard X-ray properties from the super-Eddington flow in the present study. We expect that future larger-box simulations will improve this discrepancy.

We may thus safely conclude that the success in reproducing the observed hard excess spectrum provides good support to the super-Eddington scenario for ULXs.

4.5 The effects of the photosphere

Kawashima et al. (2012) carried out the calculations for the other choices of $\tau_{\text{eff}} = 1, 3, 5, 10, 20$ for the locations of the photosphere, but confirmed that the spectrum for the photosphere $\tau_{\text{eff}} = 10$ is essentially the same as that obtained for the deeper photosphere $\tau_{\text{eff}} > 10$. We also recalculate the spectra for the case of different photosphere, i.e., $\tau_{\text{eff}} = 5, 20, 30$. The spectrum looks very similar and the fitting results are quite similar; now the best-fit parameter at $\tau_{\text{eff}} = 30$ is $\Gamma = 3.1 (+1.3/-2.1)$, in good agreement with the case with $\tau_{\text{eff}} = 10$ (see table2). For these reason, it is essentially to set photosphere $\tau_{\text{eff}} = 10$.

Acknowledgments

This work is partially supported by JSPS Grant-in-Aid for Scientific Research (C) (17K05383 S. M.; 15K05036 K.O.). Numerical computations were mainly carried out on Cray XC30 at Center for Computational Astrophysics, National Astronomical Observatory of Japan. This research was also supported by MEXT as Priority Issue on Post-K computer (Elucidation of the Fundamental Laws and Evolution of the Universe) and JICFuS.

References

Bachetti, M., Harrison, F. A., Walton, D. J., et al. 2014, *Nature*, 514, 202
 Done, C., Gierlinski, M., Kubota, A. 2007, *A&AR*, 15, 1.
 Fürst, F., Walton, D. J., Stern, D., et al. 2016, *ApJ*, 831, L14
 Gladstone, J. C., Roberts, T. P., & Done, C. 2009, *MNRAS*, 397, 1836
 Gu, W.-M., Sun, M.-Y., Lu, Y.-J., Yuan, F., & Liu, J.-F. 2016, *ApJ*, 818, L4

Israel G. L., Belfiore, A., Stella, L., et al., 2017, *MNRAS*, 466, 48
 Jiang, Y.-F., Stone, J. M., Davis, S. W. 2014, *ApJ*, 796, 106
 Kato, S., Fukue, J., Mineshige, S., 2008, *Black-Hole Accretion disks – Towards a New Paradigm* (Kyoto: Kyoto University Press)
 Kawashima, T., Ohsuga, K., Mineshige, S., et al. 2009, *PASJ*, 61, 769
 Kawashima, T., Ohsuga, K., Mineshige, S., et al. 2012, *ApJ*, 752, 18-29
 King, A. R., Davies, M. B., Ward, M. J., Fabbiano, G., & Elvis, M. 2001, *ApJ*, 552, L109
 Levermore, C. D., & Pomraning, G. C. 1981, *ApJ*, 248, 321
 Makishima, K., Kubota, A., Mizuno, T., et al. 2000, *ApJ*, 535, 632
 Makishima, K., 2007, in *IAU Symp. 238, Black Holes from Stars to Galaxies Across the Range of Masses*, ed. V. Karas & G. Matt (Cambridge, UK: Cambridge University Press), 209
 McKinney, J. C., Tchekhovskoy, A., Sadowski, A., Narayan, R. 2014, *MNRAS*, 441, 3177
 McKinney, J. C., Chluba, J., Wielgus, M., Narayan, R., Sądowski, A., 2017, *MNRAS*, 467, 2241
 Middleton MJ, Walton DJ, Fabian A, Roberts TP, Heil L, et al. 2015b, *MNRAS*, 454, 3134
 Miller, J. M., Fabian, A. C., & Miller, M. C. 2004, *ApJ*, 614, L117
 Mineshige, S., Hirano, A., Kitamoto, S., Yamada, T. T., Fukue, J. 1994, *ApJ*, 426, 308
 Mortlock D. J., et al., 2011, *Nature*, 474, 616
 Motch, C., Pakull, M. W., Soria, R., Grisé, F., & Pietrzyński, G. 2014, *Nature*, 514, 198
 Narayan, R., Sądowski, A., Soria R., 2017, *MNRAS*, (arXiv:1702.01158)
 Ogawa, T., Mineshige, S., Kawashima, T., Ohsuga, K., & Hashizume, K. 2017, *PASJ*, 69, 33
 Ohsuga, K., Mori, M., Nakamoto, T., & Mineshige, S. 2005, *ApJ*, 628, 368
 Ohsuga, K., Mineshige, S., Mori, M., Kato, Y. 2009, *PASJ*, 61, 7
 Ohsuga, K., Mineshige, S., 2011, *ApJ*, 736, 2
 Paczyński, B., & Wiita, P. J. 1980, *A&A*, 88, 23
 Pozdnyakov, L. A., Sobol, I. M., & Siuniae, R. A. 1983, *Astrophys. Space Phys. Res.*, 2, 189
 Rybicki G. B., Lightman A. P., 1986, *Radiative Processes in Astrophysics*
 Sądowski, A., Narayan, R., Tchekhovskoy, A., Zhu, Y., 2013, *MNRAS*, 429, 3533
 Sądowski, A., Narayan, R., McKinney, J. C., & Tchekhovskoy, A. 2014, *MNRAS*, 439, 503
 Sądowski, A., Narayan, R., Tchekhovskoy, A., Abarca, D., Zhu, Y., McKinney, J. C., 2015, *MNRAS*, 447, 49
 Sądowski, A., & Narayan, R. 2015, *MNRAS*, 453, 3213
 Shakura, N. I., & Sunyaev, R. A. 1973, *A&A*, 24, 337
 Takahashi, H., Ohsuga, K., Kawashima, T., & Sekiguchi, Y. 2016, *ApJ*, 826, 23
 Turner, N. J., & Stone, J. M. 2001, *ApJS*, 135, 95
 Walton, D. J., Middleton, M. J., Rana, V., et al. 2015, *ApJ*, 806, 65
 Watarai, K., Mizuno, T., & Mineshige, S. 2001, *ApJ*, 549, L77